

## Research Article

<https://doi.org/10.1631/jzus.A2200528>



# Fractal analysis of small-micro pores and estimation of permeability of loess using mercury intrusion porosimetry

Tuo LU<sup>1,2</sup>, Yaming TANG<sup>3✉</sup>, Yongbo TIE<sup>4</sup>, Bo HONG<sup>3</sup>, Wei FENG<sup>3</sup>

<sup>1</sup>Chinese Academy of Geological Sciences, Beijing 100037, China

<sup>2</sup>School of Water Resources and Environment, China University of Geosciences, Beijing 100083, China

<sup>3</sup>Xi'an Center of China Geological Survey, Xi'an 710054, China

<sup>4</sup>Chengdu Center of China Geological Survey, Chengdu 610081, China

**Abstract:** Many popular models have been proposed to study the fractal properties of the pores of porous materials based on mercury intrusion porosimetry (MIP). However, most of these models do not directly apply to the small-micro pores of loess, which have a significant impact on the throat pores and tunnels for fluid flow. Therefore, in this study we used a combination of techniques, including routine physical examination, MIP analysis, and scanning electron microscope (SEM) image analysis, to study these small-micro pores and their saturated water permeability properties. The techniques were used to determine whether the fractal dimensions of six MIP fractal models could be used to evaluate the microstructure types and permeability properties of loess. The results showed that the Neimark model is suitable for analysis of small-micro pores. When applied to saturated water permeability, the results from this model satisfied the correlation significance test and were consistent with those from SEM analysis. A high clay content and density cause an increase in the number of small-micro pores, leading to more roughness and heterogeneity of the pore structure, and an increase in the fractal dimensions. This process further leads to a decrease in the content of macro-meso pores and saturated water permeability. Furthermore, we propose new parameters: the \*Ellipse and its area ratios (\*EAR). These parameters, coupled with 2D-SEM and 3D-MIP fractal dimensions, can effectively and quantitatively be used to evaluate the types of loess microstructures (from type I to type III) and the saturated water permeability (magnitude from  $1 \times 10^{-4}$  cm/s to  $1 \times 10^{-5}$  cm/s).

**Key words:** Malan loess; Fractal models; Small-micro pores; Mercury intrusion porosimetry (MIP); Microstructure; Saturated water permeability


## 1 Introduction

The Belt and Road Strategy and the Great Western Development policies in China have led to an increase in urban development on the Loess Plateau, which is the thickest loess deposit in the world, covering more than 440000 km<sup>2</sup> (Zhu et al., 1983; Ma et al., 2017). The impact of pore structure on hydraulic and permeability properties during civil engineering activities in plateau regions with abundant loess is becoming increasingly noticeable (Li and Li, 2017; Li et al., 2018; Mu et al., 2020; Zhang et al., 2020; Xu et al.,

2022; Yu et al., 2022). Small-micro pores are an essential component of loess pore structure. They include some inter-aggregate pores and intra-aggregate pores, which have been described as narrow sluices and throat pores allowing fluid flow (Li and Li, 2017; Li et al., 2018; Wei et al., 2019a, 2019b, 2020b). However, it is not easy to precisely quantify the geometric characteristics of these pores, such as the pore size distribution (PSD), using conventional statistical methods based on mercury intrusion porosimetry (MIP). Nevertheless, the fractal hypothesis provides a new method to quantify some parameters of these pores (Pfeifer and Avnir, 1983).

In previous studies, six different fractal models based on the fractal hypothesis have been proposed. Their results closely match estimates of material heterogeneity obtained from the MIP data of sands, coals, and clayey soils (Friesen and Mikula, 1987;

✉ Yaming TANG, tangyaming@mail.cgs.gov.cn

 Yaming TANG, <https://orcid.org/0000-0002-6368-9410>

Received Nov. 9, 2022; Revision accepted Feb. 21, 2023;  
Crosschecked June 14, 2023

© Zhejiang University Press 2023

Neimark, 1992; Shen et al., 1995; Zhang and Li, 1995; Li and Horne, 2006; Li, 2010; Zhang and Weller, 2014). However, the results from various fractal models are not always consistent and the small-micro porosity fractal region of materials is likely to have a single fractal dimension for most MIP fractal models (Zhang and Weller, 2014; Li et al., 2017; Zhou and Tang, 2018; Hu et al., 2020; Dou et al., 2021; Xiao et al., 2022).

Meanwhile, it has been pointed out that a fractal region with a ratio of pores (the minimum diameter to the maximum diameter) smaller than  $1 \times 10^{-3}$  ( $d_{\min} \ll d_{\max}$ ) should be given more consideration so that the calculated fractal dimension has a representative and fractal scaleless band in a porous material (Mandelbrot, 1982; Yu and Li, 2001).

A few studies based on MIP tests have been carried out on the fractal characteristics of intact Malan loess pores. Questions remain as to whether small-micro pores have a robust fractal feature, and which existing fractal models are suitable for characterizing them. Thus, in this study we performed a systematic comparative analysis of six popular fractal models using MIP, scanning electron microscopy (SEM), and routine laboratory tests (soil natural density test, natural water content test, specific gravity test, soil particle size screening test, liquid plastic limit test,

double-oedometer method estimating the collapsibility of loess test, and the falling water head permeability test), to analyze the fractal characteristics of the small-micro pores of loess, their microstructure, and their saturated water permeability. We aimed to determine if the existing fractal models were applicable to the small-micro pores of loess, and whether the results of fractal analysis correlated with the saturated water permeability. Finally, we developed a novel method that couples 2D and 3D fractal dimensions, to evaluate the microstructure and saturated water permeability properties of loess.

## 2 Fractal models

### 2.1 Fractal models based on mercury intrusion porosimetry

Fractal models based on MIP data have been classified into six prevalent models (Table 1) (Lu et al., 2022).

### 2.2 Box-counting fractal dimension

The box-counting fractal dimension (Li et al., 2009) was taken as a key reference indicator to compare results from the above-mentioned six MIP fractal models.

**Table 1** MIP fractal models considered in this study (Lu et al., 2022)

Model No.	Fractal model	Reference	Formula expression
1	Friesen-Mikula model	Pfeifer and Avnir, 1983; Friesen and Mikula, 1987	$\lg \left( \frac{\Delta V_{\text{Hg}}}{\Delta P} \right) = (D_1 - 4) \lg(P) + C_1$
2	Neimark model	Neimark, 1992	$\lg(A \leq P) = (D_2 - 2) \lg(P) + C_2$
3	Shen model	Shen et al., 1995	$\lg \left( \frac{\Delta V_{\text{Hg}}}{d^3} \right) = -D_3 \lg(d) + C_3$
4	Zhang-Li model	Zhang and Li, 1995	$\begin{cases} \sum_{i=1}^n \overline{P}_i \Delta(V_{\text{Hg}})_i = C \cdot d_n^2 \left( \frac{(V_{\text{Hg}})_n^{1/3}}{d_n} \right)^D, \\ W_n = \sum_{i=1}^n \overline{P}_i \Delta(V_{\text{Hg}})_i / d_n^2, \quad \rightarrow \lg(W_n) = D_4 \lg(Q_n) + C_4 \\ Q_n = \left( \frac{(V_{\text{Hg}})_n^{1/3}}{d_n} \right) \end{cases}$
5	Shen-Li model	Shen et al., 1995; Li and Horne, 2006; Li, 2010	$\lg(S_{\text{Hg}}) = (D_5 - 2) \lg(P) + C_5$
6	Zhang-Weller model	Zhang and Weller, 2014	$\lg(\phi_{\text{Hg}}) = (3 - D_6) \lg(d/d_{\max}) + C_6$

$P$ : mercury inlet pressure, Pa;  $\Delta P$ : difference between two adjacent  $P$  values, Pa;  $\overline{P}_i$ : mercury inlet pressure's mean value from  $P_{i-1}$  to  $P_i$ ;  $A \leq P$ : cumulative fractal surface area smaller than or equal to pressure  $P$ ,  $\text{m}^2$ ;  $C$  or  $C_m$ : a constant or the constant produced by the fitting process ( $m=1, 2, 3, \dots, 6$ );  $D$  or  $D_m$ : fractal dimension or fractal dimension calculated by different MIP fractal models ( $m=1, 2, 3, \dots, 6$ );  $d$ : pore diameter, m;  $S_{\text{Hg}}$ : mercury saturation (the pockmarks-effect has been eliminated), %;  $V_{\text{Hg}}$  or  $(V_{\text{Hg}})_n$ : cumulative volume of mercury (the pockmarks-effect has been eliminated),  $\text{m}^3/\text{g}$ ;  $\Delta V_{\text{Hg}}$ : difference between two adjacent  $V_{\text{Hg}}$  values;  $\phi_{\text{Hg}}$ : cumulative pore content measured by mercury injection, %;  $n$ : number of mercury injections;  $d_n$ : measured pore diameter when the number of mercury injections is  $n$ ;  $W_n$ : work done by entering mercury;  $Q_n$ : energy possessed by the surface when filled in pore

The calculation process of the box-counting fractal dimension was as follows: In step (a), SEM images of the samples were denoised with a median filter (including increasing the brightness and the contrast), and the edges were detected with a sobel-edge filter (Fig. 1a). Then, the images were binarized using the watershed segmentation method and the pores and grains were extracted. The blue color denotes the pores, while the white color represents the grains (Fig. 1b). In step (c), an adaptive watershed segmentation algorithm (Yu et al., 2021) was derived from the images (Fig. 1c). In step (d), the pores smaller than  $8\ \mu\text{m}$  (Fig. 1d) on the label image were selected to calculate the box-counting fractal dimension (Li et al., 2009). This method changes mainly the box size to obtain a different number of boxes occupied by the pores and to fit a linear relationship among them (Figs. 1e and 1f).

### 2.3 Fractal region of small-micro pores

For a comparative analysis of the different fractal models, test samples with the same pore size range should be delineated. This pore size range is referred to as the fractal region in this study. The pore classification rule (Lei, 1987, 1988), referenced by many researchers (Wang et al., 2019; Wei et al., 2019a, 2020a, 2020b; Li ZQ et al., 2021), was used in this study (Fig. 2). Lei (1987) considered a pore less than  $8\ \mu\text{m}$  in diameter as a small pore or a micropore in

loess (Table 2). In addition, the fractal region ratio (the minimum diameter to the maximum diameter in this region) should be smaller than  $1\times 10^{-3}$  (Mandelbrot, 1982; Yu and Li, 2001) so that the calculated fractal dimension has a representative and fractal scaleless band.

Hence,  $0.006\ \mu\text{m}$  was chosen as a starting pore diameter in the fractal region and  $8\ \mu\text{m}$  as an ending pore diameter ( $0.006\ \mu\text{m}$  was the maximum value of the minimum pore diameters of all the samples considered in this study, whereas  $8\ \mu\text{m}$  was the upper limit of small-micro pores considered by previous studies (Lei, 1987, 1988). The fractal region of the small-micro pores ranged from  $0.006\ \mu\text{m}$  to  $8\ \mu\text{m}$ , and the fractal region ratio was  $0.75\times 10^{-3}<1\times 10^{-3}$  (Yu and Li, 2001). The corresponding fractal dimensions were obtained by applying each of the six models compared in this study.

## 3 Samples and testing methods

### 3.1 Sample information and routine physical tests

Nine samples were collected from typical  $Q_3$  Malan loess profiles in the Lvliang Mountain area (Liulin, Xixian, Daning, Jixian, Lanxian, Jiaocheng, Xiaoyi, and Fenxi counties) in Shanxi Province, China. The robust exhumation was able to produce samples with dimensions of  $40\ \text{cm}\times 40\ \text{cm}\times 40\ \text{cm}$  at a sampling

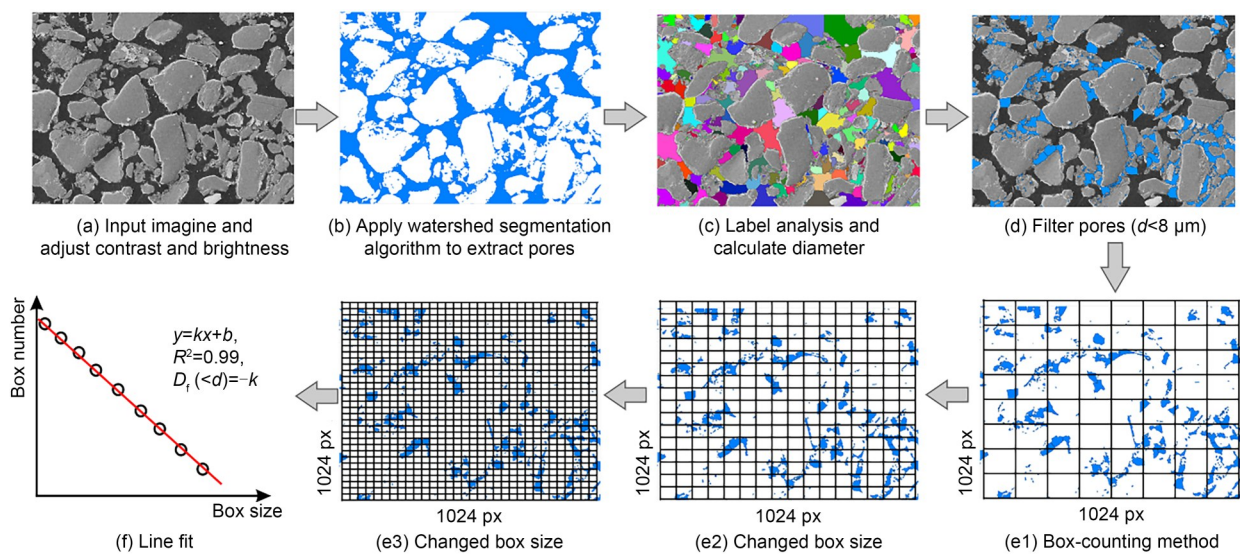


**Fig. 1** SEM image processing ((a)–(d)) and the box-counting fractal dimension calculation ((e) and (f)). Blue color represents the pores and white color represents the grains in step (b). Different colors represent different diameters in step (c).  $D_f(<d)$  is the box-counting fractal dimension, and  $k$  is the slope of the fitted straight line

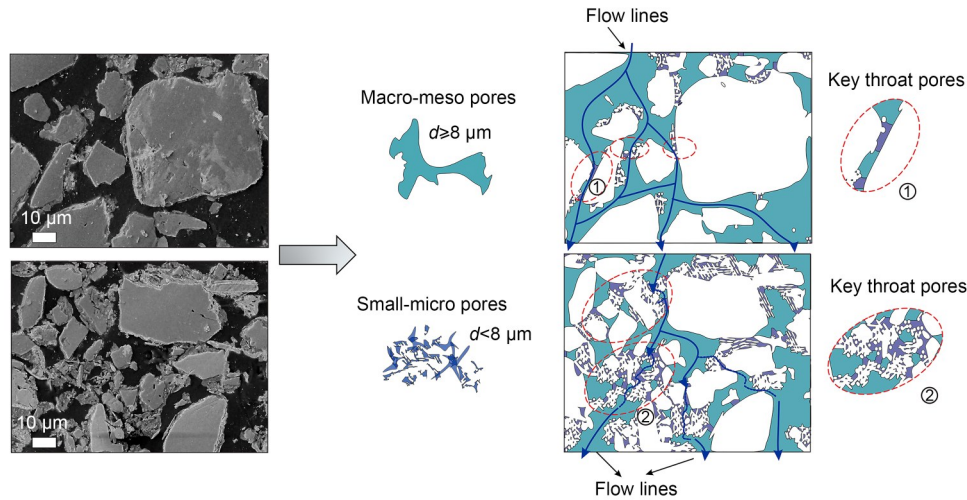


Fig. 2 Pores viewed in SEM images in this study

Table 2 Routine pore classification (Lei, 1987)

Classification	Pore size	Concept model
Macro-meso pores	$d \geq 32 \mu\text{m}$	
	$32 \mu\text{m} > d \geq 8 \mu\text{m}$	
Small-micro pores	$8 \mu\text{m} > d \geq 2 \mu\text{m}$	
	$d < 2 \mu\text{m}$	

depth of 3–10 m. The physical indices of the samples were then determined (Table 3) using the geotechnical test standard GB/T 50123-2019 (MOHURD and SAMR, 2019). The particle composition was obtained using a Bettersize 2000 laser molecule measure analyzer. The powder contained between 61.97% and 78.45% of the particles, i.e., within the range of the ordinary aeolian Malan loess.

A laboratory falling-head permeability test by TST-55 soil penetrometer (Nanjing Soil Instrument Factory, China) (6.18 cm×4.00 cm) was used to determine the saturated water permeability of the test samples.

The apparent variation among the samples from S1 to S9 was as follows (Table 3): the range in clay content was 4.58%–22.55%; the range in density was 1.47–1.68 g/cm<sup>3</sup>; the range in saturated water permeability was  $4.14 \times 10^{-5}$ – $7.72 \times 10^{-4}$  cm/s.

### 3.2 MIP and SEM tests

Water in the pore structure can affect the results when determining the pore structure of intact loess, so samples should be dried before SEM and MIP testing. Three methods are commonly used for soil drying: oven-drying (at 105 °C), freezing-drying, and air-drying. Oven-drying has the advantage of a fast-drying time. However, the rapid evaporation of water can cause damage to the soil microstructure, leading to problems such as dry cracking. Freeze-drying works on the principle of the sublimation of ice crystals and requires freezing the samples first. However, it has certain disadvantages including high cost and the likelihood of causing freeze-swelling damage to the microstructure during the freezing process. Air-drying is the process of naturally drying samples in a cold, ventilated place to minimize damage to the microstructure caused by evaporation. It is inexpensive, but the process is slow, and often takes 7–10 d to complete. Considering the pros and cons of these methods, the air-drying method was chosen for this study.



**Table 3** Physical parameters of the samples

No.	$\omega$ (%)	$\rho$ (g/cm <sup>3</sup> )	$G_s$	$C_{\text{clay}}$ (%)	$C_{\text{pores}} (<8 \mu\text{m})$ (%)	$d_{50}(\text{g})$ ( $\mu\text{m}$ )	$d_{50}(\text{p})$ ( $\mu\text{m}$ )	$I_p$ (%)	$W_L$	$a$ (MPa <sup>-1</sup> )	$\delta$	$k_s$ ( $\times 10^{-4}$ cm/s)
S1	12.34	1.54	2.67	6.58	38.15	45.21	10.59	17.27	-0.03	0.20	0.04	7.72
S2	4.30	1.47	2.68	4.58	39.07	49.71	10.28	12.15	-0.81	0.19	0.04	5.91
S3	7.77	1.47	2.69	5.49	52.62	34.13	8.99	14.89	-0.53	0.22	0.05	6.91
S4	9.39	1.55	2.68	10.60	84.82	21.48	4.64	16.35	-0.53	1.13	0.04	1.65
S5	11.01	1.54	2.68	9.00	73.75	26.95	5.14	12.99	-0.57	0.17	0.07	1.12
S6	15.89	1.56	2.67	11.24	70.77	20.91	3.48	13.63	-0.20	0.14	0.01	1.00
S7	7.01	1.61	2.67	15.90	75.25	17.71	2.16	13.15	-0.65	0.32	0.01	0.58
S8	10.72	1.59	2.70	19.15	60.78	20.52	5.32	15.73	-0.37	0.27	0.02	0.86
S9	16.10	1.68	2.68	22.55	89.88	13.78	0.94	14.04	-0.24	0.64	0.01	0.41

$\omega$  is the natural water content;  $\rho$  is the natural density;  $G_s$  is the specific gravity of the soil particles;  $C_{\text{clay}}$  is the clay content;  $C_{\text{pores}} (<8 \mu\text{m})$  is the content of pores less than 8  $\mu\text{m}$ ;  $d_{50}(\text{g})$  is the median grain diameter;  $d_{50}(\text{p})$  is the median pore diameter;  $I_p$  is the plasticity index;  $W_L$  is the liquid index;  $a$  is the coefficient of compressibility;  $\delta$  is the collapsibility coefficient;  $k_s$  is the saturated water permeability, also called the saturated hydraulic conductivity

The naturally air-dried samples were cut into cubes of 2.0 cm $\times$ 2.0 cm $\times$ 1.5 cm. Then, an Autopore IV9500 mercury porosimeter (Micromeritics company, USA) was used to perform the MIP test in accordance with Chinese standard (AQSIQ, 2012). The pressure range for the mercury porosimeter was measured to be 0.003–414 MPa. However, due to the possible presence of some visible wormholes, root holes, cracks, the rough undulations on the surface of samples, and the limited minimal pressure of the MIP apparatus, the mercury might infiltrate or mistakenly detect pores of larger diameter (Mu et al., 2020, 2022). Thus, to determine the pores within the actual structure in this study, it was necessary to avoid these mega-pores while preparing MIP test samples. Following the MIP test, the diameter of the actual largest pore was obtained by determining the threshold entry pressure (Fig. S1 of the electronic supplementary materials (ESM)),  $P_e$ , i.e., the pressure at which mercury enters the largest-diameter pore (Robinson, 1966; Pittman, 1992; AQSIQ, 2012).

The SEM test method was performed according to Li and Li (2017). The naturally air-dried loess samples were cut into cubes of 2.0 cm $\times$ 2.0 cm $\times$ 1.5 cm and covered with special glue. The test samples were cut into thin discs and polished. A JSM-7500 field emission microscope (JEOL Company, Japan) (magnification 400 $\times$ , image resolution 0.46  $\mu\text{m}$ ) was used to inspect the samples and obtain images. The box-counting fractal dimensions were calculated using the SEM images of the test samples.

## 4 Results

### 4.1 Results of fractal models

Models 1 and 6: The decision coefficient (adjusted  $R^2$ ) of the fitting equation represents the linear goodness of fit for a fractal curve. A better linear fit suggests better fractal properties, and the linear fit is good when the decision coefficient is close to 1.0. The fractal curves of Models 1 and 6 showed a somewhat poor linear fit in the fractal regions. The fractal curves of Model 1 started to fall steadily from 5.680  $\mu\text{m}$  (Fig. S2 of the ESM); therefore, its fractal region was practically 0.006–5.680  $\mu\text{m}$ . The fractal curves of Model 6 exhibited more curvilinear features than straight lines (Fig. S3 of the ESM). Hence, the fractal property of Model 1 was better than that of Model 6, according to the decision coefficients (Fig. 3a, Table 4). The fractal dimension ranges ( $D_1$  and  $D_6$ ) of Models 1 and 6 in the fractal region were 2.69–2.83 and 2.40–2.60, respectively.

Models 2 and 5: These models had similar inflection points of around 8.0  $\mu\text{m}$  on their fractal curves (Figs. S4 and S5). Furthermore, the linear fit of Model 2 was much better than that of Model 5. The fractal dimension range in the fractal region was 2.59–2.98 for Model 2 ( $D_2$ ), and was 2.04–2.25 for Model 5 ( $D_5$ ) (Fig. 3a, Table 4).

Models 3 and 4: these models had no noticeable inflection points on their fractal curves and seemingly had single fractal dimensions (Figs. S6 and S7). Furthermore, their fractal properties were better than those

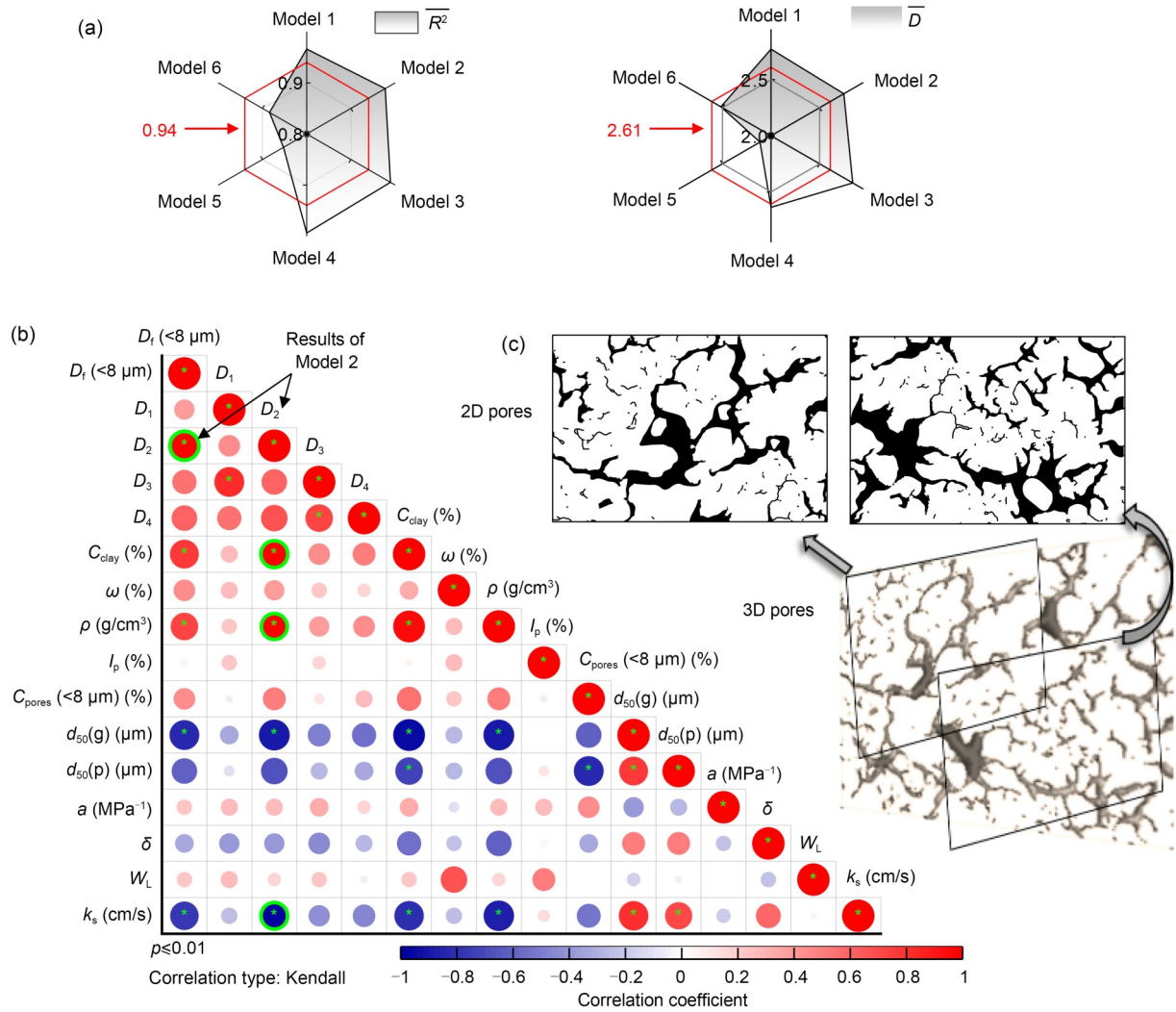


**Fig. 3** Correlation analysis: (a) the averages of adjusted  $R^2$  and  $D$  values for each model; (b) correlations between fractal dimensions and physical properties (the green circles represent suitable fractal models and key physical parameters, e.g., saturated water permeability); (c) relationship between 3D and 2D pore structures

**Table 4** Fractal results

No.	Model 1		Model 2		Model 3		Model 4		Model 5		Model 6		Box-counting method	
	$R^2$	$D_1$	$R^2$	$D_2$	$R^2$	$D_3$	$R^2$	$D_4$	$R^2$	$D_5$	$R^2$	$D_6$	$R^2$	$D_f$
S1	0.98	2.77	0.97	2.61	0.99	2.81	0.99	2.61	0.93	2.05	0.94	2.56	0.99	1.46
S2	0.97	2.73	0.94	2.59	0.98	2.78	0.99	2.60	0.88	2.04	0.82	2.47	0.99	1.44
S3	0.98	2.78	0.99	2.66	0.99	2.84	0.99	2.61	0.90	2.07	0.95	2.57	0.99	1.45
S4	0.97	2.69	0.98	2.71	0.99	2.75	0.99	2.57	0.70	2.11	0.87	2.46	0.99	1.52
S5	0.96	2.73	0.97	2.75	0.99	2.79	0.99	2.62	0.81	2.10	0.84	2.50	0.99	1.52
S6	0.98	2.73	0.99	2.77	0.99	2.81	1.00	2.61	0.81	2.12	0.90	2.52	0.99	1.60
S7	0.95	2.75	0.98	2.84	0.99	2.85	1.00	2.64	0.81	2.16	0.85	2.41	0.99	1.60
S8	0.97	2.86	0.99	2.85	0.99	2.95	1.00	2.74	0.96	2.11	0.87	2.56	0.99	1.63
S9	0.94	2.91	0.99	2.98	0.99	3.00	1.00	2.72	0.87	2.25	0.93	2.60	0.99	1.69
Average	0.97	2.77	0.98	2.75	0.99	2.84	0.99	2.64	0.85	2.11	0.88	2.52	0.99	1.55

$\overline{R^2} = 0.94$ , where  $\overline{R^2}$  is the mean of all the  $R^2$  values of the test samples based on the six MIP fractal models;  $\overline{D} = 2.61$ , where  $\overline{D}$  is the mean of all the  $D$  values of the test samples based on the six MIP fractal models

of the other models based on their decision coefficients (Fig. 3a, Table 4). However, their fractal dimension values ( $D_3$  and  $D_4$ ) were different. The range of fractal dimensions in the fractal region was 2.75–3.00 for Model 3 ( $D_3$ ) and was 2.67–2.74 for Model 4 ( $D_4$ ) (Fig. 3a, Table 4).

## 4.2 Suitable fractal model for small-micro pores

The results of the fractal models ( $D_1$ ,  $D_2$ ,  $D_3$ , and  $D_4$ ) were selected for the subsequent analyses to find suitable models (Fig. 3a). Their decision coefficients were greater than 0.94 (the mean of all the  $R^2$  values of the test samples based on the six MIP fractal models), suggesting that these models had better goodness of fit than Models 5 and 6.

$D_2$  (Model 2 results) had the strongest positive correlation, with a significant  $p$ -value of 0.01 (Fig. 3b). Moreover,  $D_2$  was positively correlated with clay content and density, and negatively correlated with the saturated water permeability and median particle size ( $d_{50}(g)$ ) (Fig. 3b). Note that the fractal results of Model 2 ( $D_2$ ) in the fractal region showed a strong positive correlation and an orderly upward trend with the SEM box-counting fractal dimensions ( $D_f$  ( $<8 \mu\text{m}$ )) (Figs. 3b and 4b). Hence, Model 2 was suitable for characterizing the small-micro pores in this study.

The structural characteristics of pores in 3D space are theoretically reflected in some representative 2D planes (Mandelbrot, 1982; Yu and Li, 2001). The 3D pore structure of loess with relatively uniform particle distribution can be simplified as a stack of a series of thin 2D sections (Fig. 3c). Therefore, 2D-SEM results can be used to estimate 3D-MIP fractal results, such as those from Model 2. Similar findings were obtained by Mahamud and García (2018) and Xiao et al. (2022). They used Model 2 (the Neimark model) to characterize loess and coal pores, and their fractal results were related to pore structure.

## 5 Discussion

### 5.1 Relationship between fractal dimensions and pore structure/permeability

The test samples showed visible differences in the SEM images and the MIP data. From S1 to S9, the content of larger pores decreased while those of smaller pores ( $<8 \mu\text{m}$ ) (Figs. 4a–4c) and clay grains

(Fig. 4a) increased. The results from both the box-counting method ( $D_f$ ) and Model 2 ( $D_2$ ) increased in an orderly manner from 1.44 to 1.69 and from 2.59 to 2.98 (Fig. 4b), respectively.

As the clay content increased, the dominant particles in the soil skeleton changed from silt to clay, and individual silt particles could not clearly be seen in SEM images. Clay particles tended to stick firmly to the edges of silt grains and fill the spaces between silt particles. Similar results were obtained by Liu et al. (2016) and Mu et al. (2019). Moreover, in this study, this process led to a decrease in the number of macro-meso pores and an increase in the number of small-micro pores.

The pore structure tended to be complex and heterogeneous, with an increasing proportion of small-micro pores. The pore structure also increased the surface roughness (Figs. 3c and 4a). The roughness and heterogeneity led to the 3D-MIP and 2D-SEM fractal dimensions presenting an upward trend. After all, the pore structure, and not the fractal model type, controls the fractal characteristics. Finally, this process decreased the dominant flow line and the water-saturated permeability properties.

### 5.2 Fractal dimensions and evaluation of micro-structure and permeability properties

The theoretical range of fractal dimensions is 2–3 for 3D pores and 1–2 for 2D pores (Mandelbrot, 1982; Yu and Li, 2001). A 3D fractal dimension ( $D_{3D}$ ) value (minus two) was coupled with the 2D fractal dimension ( $D_{2D}$ ) value (minus one) to form an ellipse (marked \*Ellipse) with a theoretical area of  $0-\pi$  (Fig. 5a). This \*Ellipse area ratio (\*EAR) was used to show how close it was to  $\pi$ . \*EAR =  $(D_{3D}-2) \times (D_{2D}-1) \times \pi / (1 \times 1 \times \pi) \times 100\%$ . In this study, the fractal dimensions of Model 2 ( $D_2$ ) and the SEM's box-counting fractal dimension ( $D_f$ ) were considered as the two main axes of the \*Ellipse (Fig. 5a), and the \*EAR was then calculated (Fig. 5a). To compare differences among samples, a normalization method was applied to the physical indexes (the formula was  $X' = (X - X_{\min}) / (X_{\max} - X_{\min})$ ), where  $X$  is a soil physical parameter, such as natural density, clay content, median grain diameter, median pore diameter, collapsibility coefficient, and saturated water permeability coefficient,  $X_{\min}$  is the minimum value and  $X_{\max}$  is the maximum value of the physical parameter among all the samples considered in



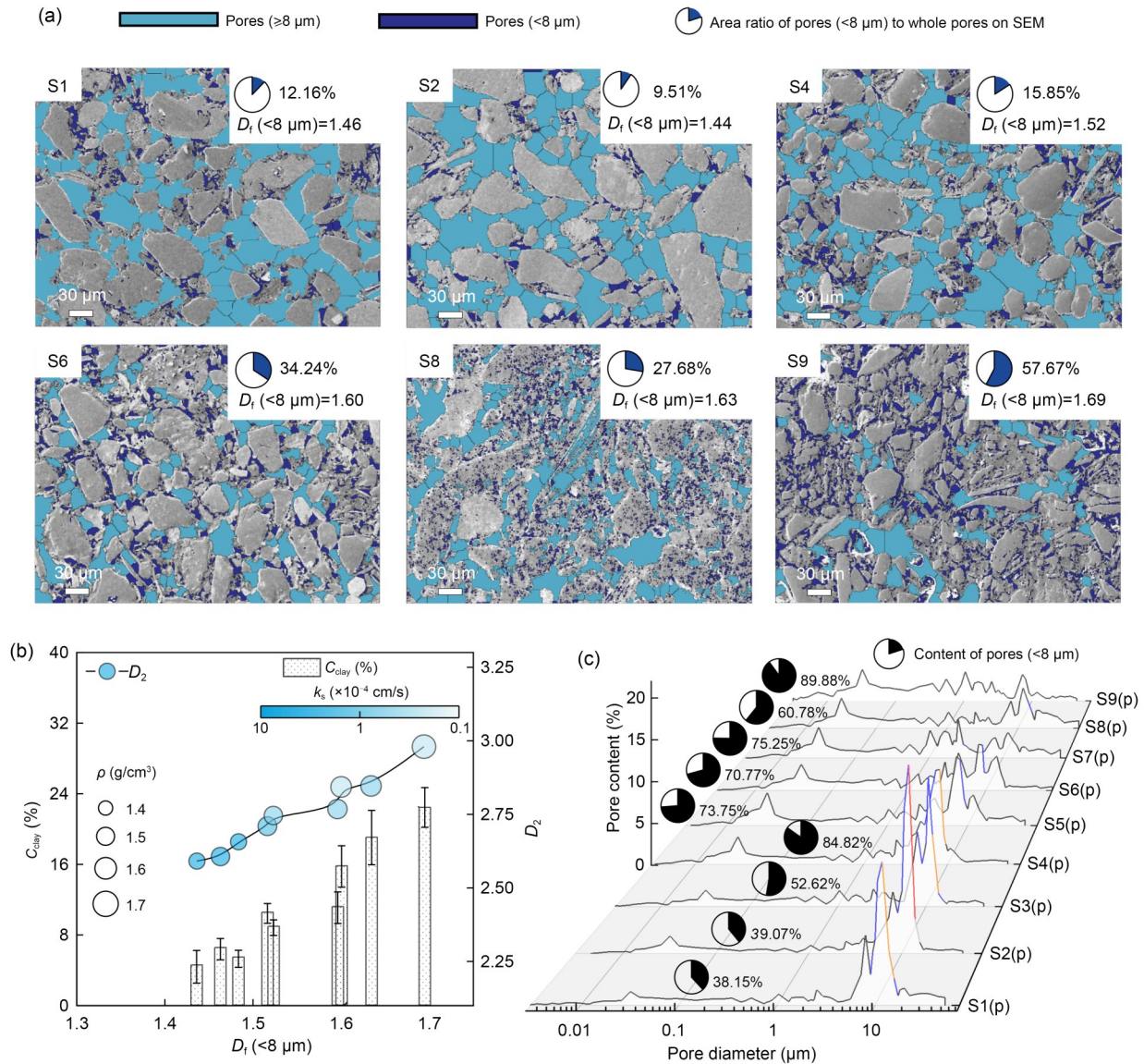


**Fig. 4** Pore (p) structure characteristics and results from Model 2: (a) pore structure of the test samples from the SEM test; (b) fractal dimensions from Model 2; (c) pore structure of the test samples from the MIP test

this study, and  $X'$  is the normalized physical parameter, as shown in Fig. 5c.

The test samples could be classified into three categories based on their clay contents and \*EAR, and corresponding to three typical microstructure types, type I, type II, and type III (Figs. 5a and 5b). The three distinct microstructure types affected saturated water permeability. In type I, the grain size distribution (GSD) and PSD curves showed typical bimodal characteristics. Clay content, density, and content of pores ( $< 8 \mu\text{m}$ ) were lower than those of the other types. In type II, the GSD and PSD curves showed typical bimodal features, while clay content, density,

and content of pores ( $< 8 \mu\text{m}$ ) were intermediate. In type III, the GSD and PSD curves showed multimodal characteristics, and clay content, density, and content of pores ( $< 8 \mu\text{m}$ ) reached a new high level (Figs. 5c and 5d).

The microstructure of the soil changed noticeably when its clay content was between 9% and 15% and its \*EAR values were between 35% and 50% (Figs. 5b and 5c). This marked the transition from type I to type II microstructure (Figs. 4b, 4c, 5c, and 5d). The saturated water permeability approached a magnitude of  $1 \times 10^{-4}$  cm/s. When the clay content was greater than 15% and the \*EAR values greater than



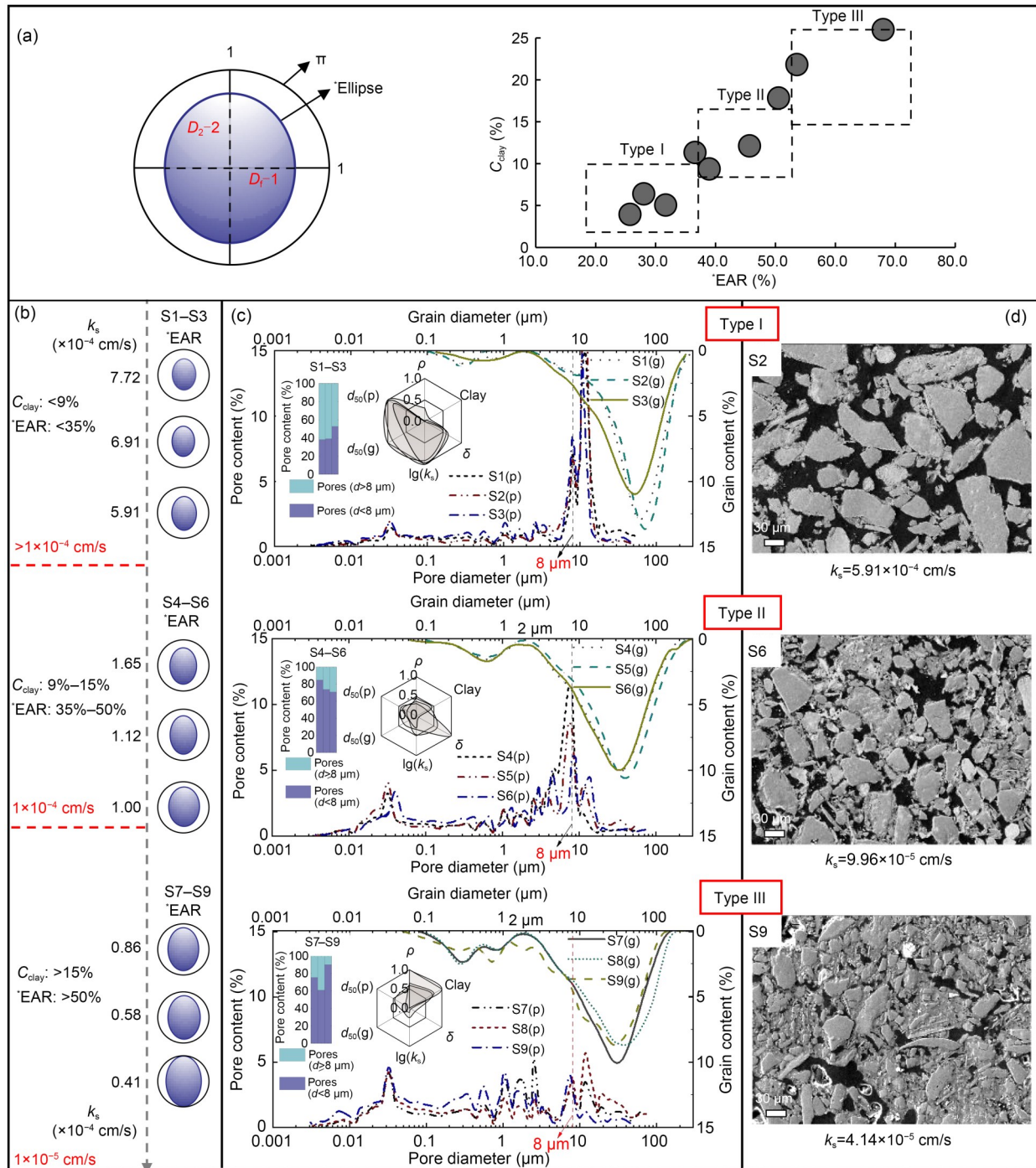


**Fig. 5** Fractal dimensions, microstructure, and permeability evaluation: (a) a new specific "Ellipse parameter" (EAR) and microstructure types; (b) EAR and saturated water permeability; (c) PSD and GSD curves and microstructure types of samples; (d) microstructure observed under SEM.  $Si(p)$ : PSD curves of test samples;  $Si(g)$ : GSD curves of test samples

50% (Figs. 5a and 5b), the microstructure ultimately transitioned from type II to type III (Figs. 4b, 4c, 5c, and 5d). This marked a steep change in saturated water permeability (from  $1 \times 10^{-4}$  cm/s to  $1 \times 10^{-5}$  cm/s)

for the loess. Notably, as the EAR value increased, the microstructure became more complex and heterogeneous and, correspondingly, the saturated water permeability declined (Figs. 5b–5d).

## 6 Conclusions

A systematic fractal analysis method, including six popular fractal models based on MIP tests, was applied to study the fractal features of small-micro pores of intact loess. In addition, some routine laboratory tests and SEM imaging were conducted to analyze the pore structure and MIP fractal results. The main findings were as follows:

(1) Model 2 (the Neimark model) of the region of the small-micro pores showed a very good linear fit (decision coefficients greater than 0.94—the average of all MIP fractal models). The results showed a strong positive correlation with clay content, density, and saturated water permeability, and followed an orderly upward trend that matched that of the box-counting fractal dimensions of SEM images.

(2) A high content of clay particles leads to an increase in the number of small-micro pores. These small-micro pores also cause more surface roughness and heterogeneity in the pore structure, which tends to present large fractal dimensions. This process leads to a decrease in the content of macro-meso pores and the dominant flow line, thereby degrading the saturated water permeability properties.

(3) A new "Ellipse and its area ratio" (EAR) parameter were introduced in this study, in which the two main half-axes consist of the Neimark model's results (minus two) and the box-counting fractal dimensions (minus one). The EAR and clay content can be used as valid parameters to quantitatively evaluate the type of loess microstructure and the saturated water permeability. The loess microstructure transitions from type I to type II when the EAR is between 35% and 50% and the clay content is between 9% and 15%. The microstructure further transitions from type II to type III when the EAR is greater than 50% and the clay content is greater than 15%. Correspondingly, the saturated water permeability shows a downward trend in magnitude from  $1 \times 10^{-4}$  cm/s to  $1 \times 10^{-5}$  cm/s. These results can serve as reference values for the classification of the soil microstructure, seepage failure, and water storage of loess in the field of civil engineering.

## Acknowledgments

This work is supported by the China Geological Survey Project (No. DD20190642) and the Shaanxi Provincial Key Research Program of China (No. 2019ZDLSF07-07-02).

## Author contributions

Yaming TANG designed the research. Tuo LU, Bo HONG, and Wei FENG processed the corresponding data. Tuo LU wrote the first draft of the manuscript. Yongbo TIE helped to organize the manuscript. Yaming TANG revised and edited the final version.

## Conflict of interest

Tuo LU, Yaming TANG, Yongbo TIE, Bo HONG, and Wei FENG declare that they have no conflict of interest.

## References

- AQSIQ (General Administration of Quality Supervision, Inspection and Quarantine of the People's Republic of China), 2012. Rock Capillary Pressure Measurement, GB/T 29171-2012. National Standards of the People's Republic of China (in Chinese).
- Dou WC, Liu LF, Jia LB, et al., 2021. Pore structure, fractal characteristics and permeability prediction of tight sandstones: a case study from Yanchang formation, Ordos basin, China. *Marine and Petroleum Geology*, 123:104737. <https://doi.org/10.1016/j.marpetgeo.2020.104737>
- Friesen WI, Mikula RJ, 1987. Fractal dimensions of coal particles. *Journal of Colloid and Interface Science*, 120(1): 263-271. [https://doi.org/10.1016/0021-9797\(87\)90348-1](https://doi.org/10.1016/0021-9797(87)90348-1)
- Hu YB, Guo YH, Shangguan JW, et al., 2020. Fractal characteristics and model applicability for pores in tight gas sandstone reservoirs: a case study of the upper paleozoic in Ordos basin. *Energy & Fuels*, 34(12):16059-16072. <https://doi.org/10.1021/acs.energyfuels.0c03073>
- Lei XY, 1987. Pore types and collapsibility of Chinese loess. *Science in China Series B-Chemistry, Biological, Agricultural, Medical & Earth Sciences*, 17(12):1309-1318 (in Chinese).
- Lei XY, 1988. The types of loess pores in China and their relationship with collapsibility. *Science in China Series B-Chemistry, Biological, Agricultural, Medical & Earth Sciences*, 18(11):1398-1411 (in Chinese).
- Li J, Du Q, Sun CX, 2009. An improved box-counting method for image fractal dimension estimation. *Pattern Recognition*, 42(11):2460-2469. <https://doi.org/10.1016/j.patcog.2009.03.001>
- Li KW, 2010. Analytical derivation of brooks-corey type capillary pressure models using fractal geometry and evaluation of rock heterogeneity. *Journal of Petroleum Science and Engineering*, 73(1-2):20-26. <https://doi.org/10.1016/j.petrol.2010.05.002>
- Li KW, Horne RN, 2006. Fractal modeling of capillary pressure curves for the geysers rocks. *Geothermics*, 35(2):198-207. <https://doi.org/10.1016/j.geothermics.2006.02.001>
- Li P, Zheng M, Bi H, et al., 2017. Pore throat structure and fractal characteristics of tight oil sandstone: a case study in the Ordos basin, China. *Journal of Petroleum Science and Engineering*, 149:665-674.

- <https://doi.org/10.1016/j.petrol.2016.11.015>
- Li XA, Li LC, 2017. Quantification of the pore structures of Malan loess and the effects on loess permeability and environmental significance, Shaanxi Province, China: an experimental study. *Environmental Earth Sciences*, 76(15): 523.  
<https://doi.org/10.1007/s12665-017-6855-7>
- Li YR, He SD, Deng XH, et al., 2018. Characterization of macropore structure of Malan loess in NW China based on 3D pipe models constructed by using computed tomography technology. *Journal of Asian Earth Sciences*, 154: 271-279.  
<https://doi.org/10.1016/j.jseaes.2017.12.028>
- Li ZQ, Qi SW, Qi ZY, et al., 2021. Microstructural insight into the characteristics and mechanisms of compaction during natural sedimentation and man-made filling on the Loess Plateau. *Environmental Earth Sciences*, 80(19):668.  
<https://doi.org/10.1007/s12665-021-09980-1>
- Liu Z, Liu FY, Ma FL, et al., 2016. Collapsibility, composition, and microstructure of loess in China. *Canadian Geotechnical Journal*, 53(4):673-686.  
<https://doi.org/10.1139/cgj-2015-0285>
- Lu T, Tang YM, Ren HY, et al., 2022. A new method to determine the segmentation of pore structure and permeability prediction of loess based on fractal analysis. *Bulletin of Engineering Geology and the Environment*, 81:509.  
<https://doi.org/10.1007/s10064-022-03016-z>
- Ma FL, Yang J, Bai XH, 2017. Water sensitivity and microstructure of compacted loess. *Transportation Geotechnics*, 11:41-56.  
<https://doi.org/10.1016/j.trgeo.2017.03.003>
- Mahamud MM, García V, 2018. Textural characterization of chars using fractal analysis of N<sub>2</sub> and CO<sub>2</sub> adsorption. *Fuel Processing Technology*, 169:269-279.  
<https://doi.org/10.1016/j.fuproc.2017.10.013>
- Mandelbrot BB, 1982. *The Fractal Geometry of Nature*. W. H. Freeman, San Francisco, USA.
- MOHURD (Ministry of Housing and Urban-Rural Development of the People's Republic of China), SAMR (State Administration for Market Regulation of the People's Republic of China), 2019. Standard for Geotechnical Testing Method, GB/T 50123-2019. National Standards of the People's Republic of China (in Chinese).
- Mu QY, Ng CWW, Zhou C, et al., 2019. Effects of clay content on the volumetric behavior of loess under heating-cooling cycles. *Journal of Zhejiang University-SCIENCE A (Applied Physics & Engineering)*, 20(12):979-990.  
<https://doi.org/10.1631/jzus.A1900274>
- Mu QY, Zhou C, Ng CWW, 2020. Compression and wetting induced volumetric behavior of loess: macro- and micro-investigations. *Transportation Geotechnics*, 23:100345.  
<https://doi.org/10.1016/j.trgeo.2020.100345>
- Mu QY, Dong H, Liao HJ, et al., 2022. Effects of in situ wetting-drying cycles on the mechanical behaviour of an intact loess. *Canadian Geotechnical Journal*, 59(7): 1281-1284.  
<https://doi.org/10.1139/cgj-2020-0696>
- Neimark A, 1992. A new approach to the determination of the surface fractal dimension of porous solids. *Physica A: Statistical Mechanics and Its Applications*, 191(1-4):258-262.  
[https://doi.org/10.1016/0378-4371\(92\)90536-Y](https://doi.org/10.1016/0378-4371(92)90536-Y)
- Pfeifer P, Avnir D, 1983. Chemistry in noninteger dimensions between two and three. I. Fractal theory of heterogeneous surfaces. *The Journal of Chemical Physics*, 79(7): 3558-3565.  
<https://doi.org/10.1063/1.446210>
- Pittman ED, 1992. Relationship of porosity and permeability to various parameters derived from mercury injection-capillary pressure curves for sandstone. *AAPG Bulletin*, 76(2):191-198.  
<https://doi.org/10.1306/BDF87A4-1718-11D7-8645000102C1865D>
- Robinson RB, 1966. Classification of reservoir rocks by surface texture. *AAPG Bulletin*, 50(3):547-559.  
<https://doi.org/10.1306/5D25B4A7-16C1-11D7-8645000102C1865D>
- Shen P, Li K, Jia F, 1995. Quantitative description for the heterogeneity of pore structure by using mercury capillary pressure curves. International Meeting on Petroleum Engineering.  
<https://doi.org/10.2118/29996-MS>
- Wang JD, Li P, Ma Y, et al., 2019. Evolution of pore-size distribution of intact loess and remolded loess due to consolidation. *Journal of Soils and Sediments*, 19(3):1226-1238.  
<https://doi.org/10.1007/s11368-018-2136-7>
- Wei TT, Fan W, Yu NY, et al., 2019a. Three-dimensional microstructure characterization of loess based on a serial sectioning technique. *Engineering Geology*, 261:105265.  
<https://doi.org/10.1016/j.enggeo.2019.105265>
- Wei TT, Fan W, Yuan WN, et al., 2019b. Three-dimensional pore network characterization of loess and paleosol stratigraphy from South Jingyang Plateau, China. *Environmental Earth Sciences*, 78(11):333.  
<https://doi.org/10.1007/s12665-019-8331-z>
- Wei YN, Fan W, Yu B, et al., 2020a. Characterization and evolution of three-dimensional microstructure of Malan loess. *CATENA*, 192:104585.  
<https://doi.org/10.1016/j.catena.2020.104585>
- Wei YN, Fan W, Yu NY, et al., 2020b. Permeability of loess from the South Jingyang Plateau under different consolidation pressures in terms of the three-dimensional microstructure. *Bulletin of Engineering Geology and the Environment*, 79(9):4841-4857.  
<https://doi.org/10.1007/s10064-020-01875-y>
- Xiao T, Li P, Shao SJ, 2022. Fractal dimension and its variation of intact and compacted loess. *Powder Technology*, 395:476-490.  
<https://doi.org/10.1016/j.powtec.2021.09.069>
- Xu PP, Qian H, Zhang QY, et al., 2022. Investigating saturated hydraulic conductivity of remolded loess subjected to CaCl<sub>2</sub> solution of varying concentrations. *Journal of Hydrology*, 612:128135.  
<https://doi.org/10.1016/j.jhydrol.2022.128135>
- Yu B, Fan W, Dijkstra TA, et al., 2021. Heterogeneous evolution of pore structure during loess collapse: insights from X-ray



- micro-computed tomography. *CATENA*, 201:105206.  
<https://doi.org/10.1016/j.catena.2021.105206>
- Yu BM, Li JH, 2001. Some fractal characters of porous media. *Fractals*, 9(3):365-372.  
<https://doi.org/10.1142/S0218348X01000804>
- Yu JR, Zhou C, Mu QY, 2022. Numerical investigation on light non-aqueous phase liquid flow in the vadose zone considering porosity effects on soil hydraulic properties. *Vadose Zone Journal*, 21(5):e20211.  
<https://doi.org/10.1002/vzj2.20211>
- Zhang BQ, Li SF, 1995. Determination of the surface fractal dimension for porous media by mercury porosimetry. *Industrial & Engineering Chemistry Research*, 34(4):1383-1386.  
<https://doi.org/10.1021/ie00043a044>
- Zhang LX, Qi SW, Ma LN, et al., 2020. Three-dimensional pore characterization of intact loess and compacted loess with micron scale computed tomography and mercury intrusion porosimetry. *Scientific Reports*, 10(1):8511.  
<https://doi.org/10.1038/s41598-020-65302-8>
- Zhang ZY, Weller A, 2014. Fractal dimension of pore-space geometry of an eocene sandstone formation. *Geophysics*, 79(6):D377-D387.  
<https://doi.org/10.1190/geo2014-0143.1>
- Zhou J, Tang YQ, 2018. Experimental inference on dual-porosity aggravation of soft clay after freeze-thaw by fractal and probability analysis. *Cold Regions Science and Technology*, 153:181-196.  
<https://doi.org/10.1016/j.coldregions.2018.06.001>
- Zhu XM, Li YS, Peng XL, et al., 1983. Soils of the loess region in China. *Geoderma*, 29(3):237-255.  
[https://doi.org/10.1016/0016-7061\(83\)90090-3](https://doi.org/10.1016/0016-7061(83)90090-3)

**Electronic supplementary materials**  
 Figs. S1–S7